Full length article

Non-reactive HiPIMS deposition of NbC$_x$ thin films: Effect of the target power density on structure-mechanical properties

A. Bahr [a,*], T. Glechner [a], T. Wojcik [a], A. Kirnbauer [b], M. Sauer [c], A. Foelske [c], O. Hunold [d], J. Ramm [d], S. Kolozsvári [e], E. Ntemou [f], E. Pitthan [f], D. Primetzhofer [f], H. Riedl [a,b], R. Hahn [a]

[a] *Christian Doppler Laboratory for Surface Engineering of High-performance Components, TU Wien, Austria*
[b] *Institute of Materials Science and Technology, TU Wien, Austria*
[c] *Analytical Instrumentation Center, TU Wien, Austria*
[d] *Oerlikon Balzers, Oerlikon Surface Solutions AG, Liechtenstein*
[e] *Plansee Composite Materials GmbH, Germany*
[f] *Department of Physics and Astronomy, Uppsala University, Sweden*

A B S T R A C T

The exceptional mechanical properties of transition metal carbide coatings are known to be governed by the carbon content and its morphological distribution. Here, we verify the influence of the target peak power density on the chemical composition, microstructure, and mechanical properties of NbC$_x$ coatings grown by non-reactive high-power impulse magnetron sputtering (HiPIMS). By tuning the pulse parameters, the power density can be increased from 0.11 to 1.48 kW/cm^2 leading to a decrease in the C/Nb ratio from 1.52 to 0.99 within the films – proven by combined elastic backscattering and time-of-flight elastic recoil detection analysis. This decrease in the C/Nb ratio is accompanied by microstructural changes from nanocomposite morphologies with an average grain size of 6.6 ± 2.5 nm at 0.13 kW/cm^2 into more columnar structures with an average column width of 65.2 ± 18.7 nm at 1.48 kW/cm^2. Independent from the C/Nb ratio, all films exhibit a single face-centered cubic structure. The mechanical properties correlate with the enhanced growth behavior dominated by ions at higher peak power densities and the varied C/Nb ratios. A maximum in hardness and fracture toughness of H = 38.7 ± 3.6 GPa and K_{Ic} = 2.78 ± 0.13 MPa•m$^{1/2}$ (at 3.2 GPa residual compressive stress), is obtained for the nearly stoichiometric NbC coating exhibiting C/Nb ratio of 1.06.

1. Introduction

Transition metal carbides (TMCs) are refractory materials possessing extremely high melting temperatures (T$_M$), outstanding mechanical strength, excellent electrical conductivity, and good chemical stability [1,2]. Based on their robust thermomechanical and chemical properties, TMCs are technologically important and used in different applications as protective coatings in machining industry, wear applications [3–8] but also as catalytic materials [9–11]. Among the TMC family, NbC, which crystallizes in the face-centred cubic (fcc) NaCl-type structure, has attracted a lot of attention as it exhibits an interesting mix of refractory properties, such as T$_M$ of 3490 °C, highest hardness and Young's modulus, and a good chemical stability [12–16]. This attractive aggregate of properties makes NbC a promising coating material to be applied on diverse high-performance components such as cutting tools [16,17],

electrical contacts [13,15], fuel cells [18], but also corrosion related applications [19].

So far, different routes have been explored to grow NbC thin films such as reactive sputtering [12,15,20], non-reactive sputtering using a single compound target [17,21], but also two elemental targets [13,22], filtered arc growth [23], electron beam deposition (EBD) [24], chemical vapor deposition (CVD) [25,26], thermo-reactive diffusion (TRD) [19], as well as laser cladding [27]. Among these routes, magnetron sputtering allows the most distinct control of the thermomechanical properties through varying process parameters. Typically, sputter-deposited NbC films exhibit a nanocomposite structure comprised of nanocrystalline sub-stoichiometric carbide phases (nc-NbC$_x$) embedded in an amorphous carbon (a-C) matrix [3,15,28]. Several studies were done to control the C/Nb ratio and hence the microstructure, to influence the mechanical properties of the coatings. Yate et al. deposited NbC films

---

with a nanocomposite morphology and C content ranging from 10 to 86 at. % in non-reactive sputtering process using elemental targets [22]. The mechanical properties of the films were strongly influenced by the morphology as well as the free C content (amorphous C bonded as C—C), whereas a maximum hardness of 23 GPa was reported for the film with only 9 % free carbon phase [22]. Nedfors et al. deposited NbC coatings both reactively and non-reactively [13,15]. All their coatings consisted of nc-NbC$_x$ grains embedded in an amorphous C matrix. The grain size for the reactively sputtered coatings was in the range of 3–10 nm compared to 3–75 nm for the non-reactive coatings. Moreover, the hardness of the coatings was reduced with increasing total C content and a maximum hardness of 23 GPa was reported for a nearly stoichiometric C/Nb ratio of about 0.9 to 1 [15]. Recently, Sala et al. deposited NbC via reactive pulsed magnetron sputtering utilizing a relatively large pulse duty cycle of 28 % and frequency of 4 kHz [20]. These coatings exhibited hardness values of 10–11 GPa compared to 18–20 GPa for their DC grown counterparts. They attributed this drop in hardness to the high amorphous C fraction within the coatings and an under-dense morphology [20]. Nevertheless, the usage of pulsed growth techniques (especially those providing strongly ionized plasmas) constitute strong benefits when coming to the available energy during film growth to form highly crystalline structures [29].

As shown by Lewin and Jansson [28], the strong tendency of C to form amorphous grain boundary phases can be suppressed by providing highly energetic sputter flux, whereas high power impulse magnetron sputtering (HiPIMS) represents a valuable tool. In HiPIMS plasmas, the degree of ionization is based on the high peak power densities of up to several kW/cm^2 obtained through short pulses with small pulse duty cycles (<10 %) [30–33]. Consequently, a large flux of energetic ions and an intense bombardment of the growing film can enable the growth of highly dense but also metastable phases, controlling the film composition, microstructure and mechanical properties via the pulse parameters [34–39]. In HiPIMS, the target peak power density can be controlled while keeping the time-averaged power constant by tuning the pulse duty cycle (t$_{on}$/T) and pulse frequency (f) [30,33]. Bakhit et al. showed that the stoichiometry of TiB$_x$ films could be controlled in HiPIMS successfully by varying the B/Ti ratio in the films between 1.8 and 2.0 by controlling the pulse length (t$_{on}$) [34]. Similarly, J.C. Sánchez-López et al. controlled the stoichiometry of CrN$_x$ deposited by reactive HiPIMS by modifying the pulse parameters at constant nitrogen flow [40]. They could achieve stoichiometry variation between x = 0.63 and 1.10 within their CrN$_x$ films by changing the pulse length at a constant pulse duty cycle [40]. Soucek et al. employed reactive HiPIMS to deposit TiC coatings with high hardness (>40 GPa) and a low fraction of a-C phase [41]. In their study, the utilization of HiPIMS results in nearly stoichiometric TiC$_x$ coatings with a low a-C fraction due to the high energy influx and intense ion bombardment of the growing film in HiPIMS promoting the incorporation of carbon into TiC grains [41].

Therefore, in the present study, we thoroughly describe the HiPIMS deposition of NbC$_x$ thin films using a NbC compound target. The main focus is attributed to the influence of the peak power density on the C/Nb ratio, microstructure, and mechanical properties by varying the pulse parameters (pulse frequency, duty cycle). The chemical composition, bonding nature, and microstructure of the grown films are correlated with their mechanical properties and fracture characteristics.

2. Experimental details

All NbC thin films were synthesized using a laboratory-scaled magnetron sputtering system [42,43] using a powder metallurgically fabricated 3-inch NbC (1:1) compound target (Plansee Composite Materials GmbH, purity 99.8 %). The depositions were carried out in a pure Ar atmosphere (f$_{Ar}$ = 21 sccm) at a working gas pressure of 0.4 Pa and substrate temperature of 600 °C. The base pressure prior to the depositions was maintained below 10^{-4} Pa. A substrate bias potential of −50 V was applied in DC mode, and the substrate holder was rotated

with a frequency of 15 rpm while mounted parallel to the target at a distance of 85 mm.

The cathode was connected to a MELEC SIPP pulse generator powered by an ADL DC generator (3 kW). The target peak power density was varied from 0.11 kW/cm^2 to approximately 1.48 kW/cm^2 while utilizing a constant time-averaged power of 400 W. This variation was achieved and controlled through the pulse duty cycle (t$_{on}$/T), which was changed stepwise from 10 % to 1.5 % for frequencies of 200, 500, and 1000 Hz, respectively. Thus, to obtain a duty cycle of 10 % for 500 and 1000 Hz pulse frequencies, the pulse width was set to 200 and 100 μs, respectively. The deposition rate of the films varied between 14.2 and 34.6 nm/min, and the obtained film thicknesses range between 1.7 and 3.1 μm. All the deposition parameters are summarized in Table 1. The waveforms of the discharge voltage (V$_T$) and current (I$_T$) were recorded using a digital oscilloscope (PicoScope 6403C, Pico Technology) utilizing a voltage (Testec TT-HV 150) and current (Tektronix TCP303) probe. Moreover, the discharge peak power density within a period was calculated as

$$P_{pk} = max\left(\frac{U_T(t) \cdot I_D(t)}{A_T}\right) \tag{1}$$

where (U$_T$) and (I$_D$) are the target peak voltage and discharge peak current, respectively, and (A$_T$) is the target surface area.

All the coatings were deposited on single crystalline Si platelets (100-oriented, 20 × 7 × 0.38 mm^3), single-crystalline SiC (20 × 7 × 0.35 mm^3), single-crystalline Al$_2$O$_3$ platelets (10$\bar{1}$1-oriented, 10 × 10 × 0.53 mm^3), and polished austenitic stainless-steel platelets (20 × 7 × 0.8 mm^3). Prior to the depositions, the substrate materials were cleaned in an ultrasonic bath using acetone and ethyl alcohol consecutively. Additionally, the substrates were Ar$^+$ etched for 10 min at 5 Pa and a bias voltage of −800 V.

The chemical composition of all coatings was investigated by ion beam analysis employing elastic backscattering spectroscopy (EBS) and time-of-flight elastic recoil detection analysis (ToF-ERDA). ToF-ERDA was performed with 36 and 44 MeV I^{8+} primary ion beams and a recoil detection angle of 45° using the 5MV 15-SDH2 pelletron accelerator at Uppsala University [44]. Depth profiles of the chemical composition are obtained using two software packages, CONTES [45] and Potku [46], respectively. More details on the employed detection system can be found in [47]. Furthermore, EBS was carried out with a detection angle of 170° using 4.35 MeV 4He$^+$ primary ions and employing the strong 12C(4He,4He)12C elastic resonance at ~4.260 MeV [48]. The backscattering spectra were simulated using SIMNRA software package [49], employing the information on other light species from ERDA as an input parameter [50]. The film densities were estimated based on the EBS areal densities and the cross-sectional SEM film thicknesses (see Fig. S2 in the Supplementary).

Moreover, the structure of all coatings has been analyzed by X-ray diffraction (XRD) in Bragg Brentano configuration using a Panalytical Xpert Pro MPD system equipped with Cu-K$_\alpha$ radiation source operated at 45 keV and 40 mA (wavelength λ = 1.5418 Å). Furthermore, the growth morphology for selected samples was further investigated by cross-sectional and plane-view transmission electron microscopy (TEM FEI TECNAI F20, field emission gun with 200 kV acceleration voltage) combined with selected-area electron diffraction (SAED) analysis. The TEM samples were prepared by mechanical polishing down to a thickness of 10 μm and subsequently Ar ion polishing using a PIPS II system (Gatan). The average grain size was evaluated by the intercept method from the dark-field TEM images (using the (111) and (200) reflections).

X-ray photoelectron spectroscopy (XPS) analysis was performed using a custom-built SPECS XPS-spectrometer with a monochromatic Al-K$_\alpha$ X-ray source (μFocus 350, spot size: 450 μm, Power: 70 W) and a hemispherical WAL-150 analyzer (Acceptance angle 60°). The spectra were measured after Ar-ion etching (Ar partial pressure 2•10^{-5} Pa applying a voltage of 3 kV carried out in two steps for 120 and 240 s) to

Table 1
Deposition parameters and chemical compositions obtained by EBS and ERDA for all NbC$_x$ coatings deposited.

Sample	Deposition parameters				EBS			ERDA[a]				Density [g/cm³]
	Frequency [Hz]	t_{on} [μs]	Duty cycle [%]	Peak power density [kW/cm²]	C [at. %]	Nb [at. %]	C/Nb	C [at. %]	Nb [at. %]	O [at. %]	Ar [at. %]	
1	200	250	5	0.35	60.0	39.5	1.52	59.8 ± 3	37.3 ± 2	0.6 ± 0.2	1.2 ± 0.4	5.67 ± 0.01
2	200	125	2.5	0.77	52.9	45.7	1.16	56.3 ± 3	39.1 ± 3	0.6 ± 0.3	0.7 ± 0.3	6.58 ± 0.04
3	200	75	1.5	1.41	52.8	46.8	1.13	51.2 ± 3	45.1 ± 2	0.5 ± 0.3	0.3 ± 0.3	7.57 ± 0.01
4	500	200	10	0.13	58.1	40.5	1.43	59.0 ± 3	35.5 ± 2	0.3 ± 0.2	1.0 ± 0.4	6.19 ± 0.02
5	500	100	5	0.36	58.6	41.0	1.43	58.1 ± 3	37.8 ± 3	0.3 ± 0.2	0.9 ± 0.4	6.70 ± 0.08
6	500	50	2.5	0.76	51.0	48.1	1.06	49.6 ± 2	43.9 ± 3	0.3 ± 0.1	0.5 ± 0.1	7.00 ± 0.08
7	500	30	1.5	1.48	50.0	49.5	1.01	48.9 ± 2	46.5 ± 4	0.2 ± 0.2	0.4 ± 0.2	7.01 ± 0.08
8	1000	100	10	0.11	57.8	40.8	1.42	58.0 ± 3	37.8 ± 3	0.6 ± 0.1	0.9 ± 0.1	6.25 ± 0.01
9	1000	50	5	0.38	51.3	47.3	1.08	54.8 ± 2	41.7 ± 3	0.4 ± 0.1	0.8 ± 0.1	5.99 ± 0.04
10	1000	25	2.5	0.74	50.0	48.5	1.03	51.3 ± 3	45.9 ± 3	0.4 ± 0.1	0.4 ± 0.1	6.71 ± 0.09
11	1000	15	1.5	1.24	49.2	49.4	0.99	50.3 ± 2	45.9 ± 3	0.4 ± 0.1	0.8 ± 0.1	6.76 ± 0.05

[a] Low concentration elements of Ti, W and Al were detected at <1.5 at. %.

minimize surface contaminations. The overview and detail spectra of the single elements were measured using pass-energies of 100 eV and 30 eV and an energy resolution of 1 eV and 100 meV, respectively. The spectra analysis was done using transmission corrections (as per manufacturer's specifications), Shirley-backgrounds, and sensitivity parameters after Scofield [51]. Furthermore, the binding energy value of adventitious carbon from minor surface contamination was set to 284.8 eV for charge correction.

The mechanical properties of all the coatings in terms of hardness (H) and elastic modulus (E) were investigated on single crystalline Al$_2$O$_3$ substrates by nanoindentation using an ultra-micro indentation (UMIS) system equipped with a Berkovich diamond tip. For each coating, 31 indents with indentation load varied between 3 and 45 mN were performed in a load-controlled mode, and their load-displacement curves were consequently evaluated according to Oliver and Pharr's method [52]. The loading/unloading steps were divided into 20 increments, and a holding time of 1 s was used at the maximum load. Furthermore, the indentation depths were kept below 10 % of the film thickness in order to minimize substrate interference. Moreover, the elastic modulus was determined according to Ref. [53] after fitting the elastic modulus data as a function of the penetration depth (E vs. h). Hence, the E value was taken as the y-intercept after extrapolating the data back to the zero indentation depth [53]. The E values were calculated based on Poisson's ratio of $\nu = 0.22$ [54]. Furthermore, the residual stresses of the coatings were calculated based on the modified Stoney's equation [55] and the curvature measurements of coated SiC substrates performed using optical profilometry (PS50, Nanovea). The thicknesses of the coatings used for stress measurements were determined from the SEM cross-section images.

Furthermore, micromechanical tests were performed on microcantilevers to calculate the fracture toughness of the coatings. The microcantilevers were prepared using a ThermoFisher Scios2 (FIB-SEM dual beam system) equipped with Ga$^+$ ion source. The cantilevers (see Fig. S3 in the Supplementary) were milled using a final ion beam current of 1 nA under an acceleration voltage of 30 kV. For each coating, six cantilevers were prepared. Afterwards, the prepared cantilevers were loaded at a loading rate of 10 nm/s using a displacement-controlled FemtoTools FT-NMT04, equipped with a diamond wedge tip. The microcantilever testing was done in a Zeiss Sigma 500 FEGSEM system,

which was also used to measure the fracture surface geometries required for the calculation.

The fracture toughness of the coatings was then calculated according to Matoy et al. [55]:

$$K_{IC} = \frac{F_{max}L}{Bw^{\frac{3}{2}}} \cdot f\left(\frac{a}{w}\right) \tag{2}$$

$$f\left(\frac{a}{w}\right) = 1.46 + 24.36 \left(\frac{a}{w}\right) - 47.21 \left(\frac{a}{w}\right)^2 + 75.18 \left(\frac{a}{w}\right)^3 \tag{3}$$

where (F_{max}) is the maximum load applied, (L) is the length between the initial crack and the indenter tip, (B) is the width of the cantilever, (w) is the height of the cantilever, and a is the depth of the FIB-made notch. The dimensions of the cantilever were taken according to Brinckmann et al. [56,57].

3. Results and discussions

3.1. Discharge characteristics

Fig. 1 shows the target voltage V$_T$(t) and current I$_T$(t) waveforms as a function of the time during NbC HiPIMS at 500 Hz in pure Ar atmosphere. The discharge voltage exhibits the typical rectangular shape following the ignition oscillations maintaining values around −480, −495, −630, and −645 V for pulse lengths of 200, 100, 50, and 30 μs, respectively. These pulse lengths correspond to duty cycles of 10 % (gray lines), 5 % (blue lines), 2.5 % (dark yellow lines), and 1.5 % (black lines). Furthermore, a delay in the range of a few tens of μs can be observed between the target voltage and current. This lag is related to the discharge initiation and vacuum breakdown [58]. Moreover, for the relatively short pulses up to 100 μs, the current I$_T$(t) waveforms exhibit the well-known triangular shape while reaching the peak current value at the end of the pulse. However, the current waveform at 200 μs exhibited an initial increase till it reached the peak value and plateaued with a steady-state current value till the end of the pulse. This current plateau is an indication that the plasma has reached an equilibrium concerning density and working gas heating [59]. The target peak current increases dramatically with decreasing duty cycle and t$_{on}$, ranging from 12 to 105 A as the pulse duration decreases from 200 to 30 μs.
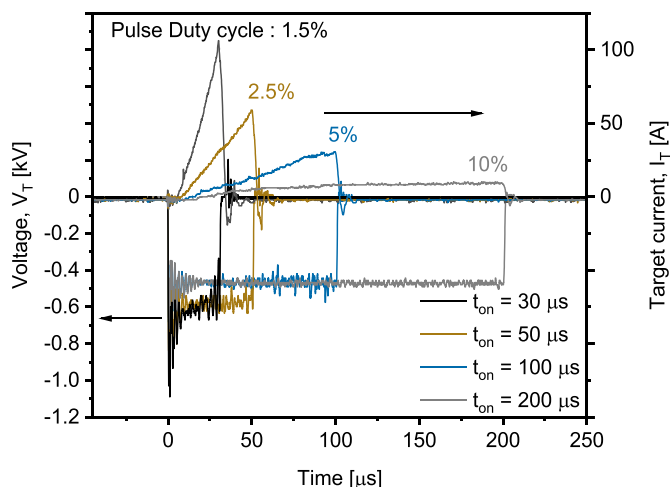
Fig. 1. Target current I_T (t) and Voltage V_T (t) waveforms as a function of the pulse length recorded during HiPIMS of NbC. The average target power was set to 400 W with a 500 Hz pulse frequency.

Consequently, the target peak power exhibits a sharp increase by shortening the pulse width.

3.2. Chemical and bonding analysis

The chemical compositions of all NbC_x films were determined by ion beam analysis employing a combination of elastic backscattering and elastic recoil detection analysis. EBS was used for an effective quantification of the distribution of Nb over the whole film thickness within the light C matrix, while ERDA provided accurate quantifications regarding all light species detectable (e.g. C, Ar, or O) [50], with EBS independently confirming the obtained C/Nb ratio for the near-surface regions.

The elemental compositions obtained by these two methods are summarized in Table 1. All films deposited at relatively low target power densities (<0.36 kW/cm^2) exhibit carbon enrichment with C/Nb > 1, whereas the residual O content is below 0.6 at. % throughout all coatings investigated. In a previous study by Liao et al. [21], overstoichiometry in carbon has been observed for NbC_x films deposited from a compound target by DCMS. Also, Mráz et al. reported a deviation in composition for Cr-Al-C thin films deposited from Cr_2AlC target, where their films were heavy-element deficient at low pressure times distance values (<20 Pa•cm) [60]. This deviation in film compositions stems from the different angular and energy emission distributions of the sputtered species [60]. Moreover, the EBS spectra of NbC_x indicate that the concentrations of film constituents are uniform along the film thickness (see also Fig. S1 in the Supplementary). Furthermore, the film densities obtained from elastic backscattering spectroscopy are included in Table 1. The NbC_x film densities exhibit a variation between 5.67 and 7.57 g/cm^3, (the density of stoichiometric bulk NbC is 7.8 g/cm^3 [61]). In correspondence to the highly ionized states within HiPIMS, the film density correlates with the applied target power density, where a film densification of even 33 % is observed by increasing the target power density. The use of HiPIMS is known to result in film densification based on the employed power densities due to the high flux ion irradiation and enhanced re-nucleation events during film growth [32,62].

Fig. 2 shows the C/Nb ratio in the grown films at different pulse frequencies as a function of the target peak power density. The C/Nb ratio in the films exhibits a clear dependence on the target peak power density, where the highest C/Nb value of 1.52 was obtained for the film deposited at 200 Hz with the power density of 350 W/cm^2. However, the C/Nb ratio decreases with increasing power density for all pulse frequencies. At the highest applied power densities, all films achieve nearly stoichiometric composition with C/Nb ratios of 0.99, 1.01, and 1.13
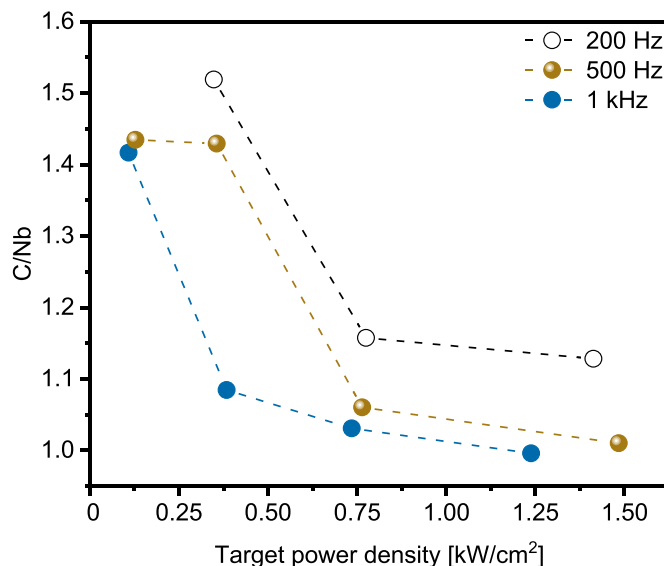

Fig. 2. The chemical composition of NbC_x thin films in terms of the C/Nb ratio as a function of the target power density. The C/Nb ratio was obtained based on the analysis done by EBS.

deposited at 1.24 kW/cm^2 at 1 kHz, 1.48 kW/cm^2 at 500 Hz, and 1.41 kW/cm^2 at 200 Hz, respectively. The reason for the drastic decrease of the carbon content by increasing power densities can be related to the ion-assisted film growth conditions during HiPIMS. The ionization fraction of the sputtered species in the HiPIMS mode strongly depends on the target power density, where higher ionization efficiencies can be achieved by increasing the target power density [31,32]. Carbon is known to have a much higher ionization potential of 11.26 eV compared to 6.75 eV for Nb [63]. Consequently, a higher ionization fraction of Nb is expected compared to C during HiPIMS. So, at low power densities, high fractions of ionized Nb are already expected in the plasma. Still, with predominant C flux of neutrals contributing to the film growth, and hence leading to a high amount of free C. By increasing the power density, more C species get ionized. The energetic C$^+$ favours the incorporation in the NbC instead of forming free C, which leads to nearly stoichiometric films at the highest applied power density (Detailed ion mass spectroscopy measurements will be part of a follow-up study). Moreover, our results are consistent with a previous study by Samuelsson et al., reporting lower free carbon contents in TiC_x grown by HiPIMS compared to DCMS coatings [3].

Fig. 3 shows the C1s XPS spectra obtained for two selected coatings deposited at the same pulse frequency of 500 Hz, but under different target peak power densities – Fig. 3a corresponds to the coating deposited at 1.48 kW/cm^2 and 3b to the one at 0.13 kW/cm^2. Deconvolution of the spectra yields two distinct components, one at 284.4 eV related to C—C bonds, whereas at 282.7 eV, Nb—C bonds are identified [13,15]. Both coatings contain a certain amount of free amorphous carbon (a-C) phase in addition to the crystalline NbC_x. Estimating the amount of the amorphous carbon based on the XPS spectra, the a-C phase decreases from 37 % to 20 % when the target power density increases from 0.13 to 1.48 kW/cm^2. The amount of free carbon in the films is correlated to the C/Nb ratio, and both are influenced by the applied target peak power density, whereas a lower content of free C is expected at higher peak power densities. Furthermore, it must be considered that during XPS measurements, not all C contamination can be removed by the Ar$^+$ pre-sputtering steps, and 5–10 at. % of C can still be expected in the analysis. Moreover, the observation of the free a-C phase is in line with many previous studies on NbC and other TMC_x coatings reporting dual-phase coatings containing sub-stoichiometric TMC_x crystals in an amorphous carbon matrix [3,13,15,22].
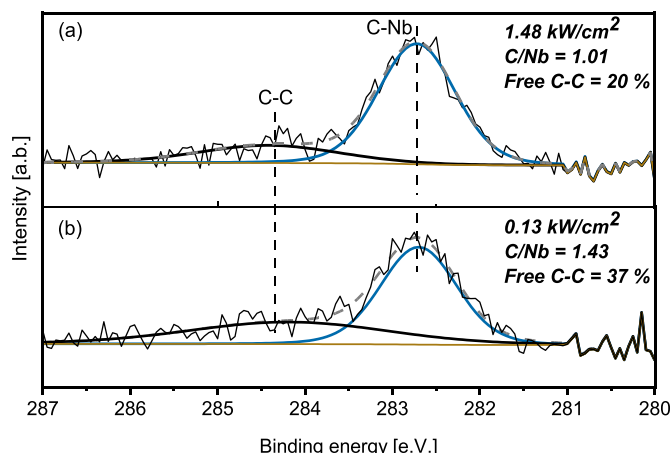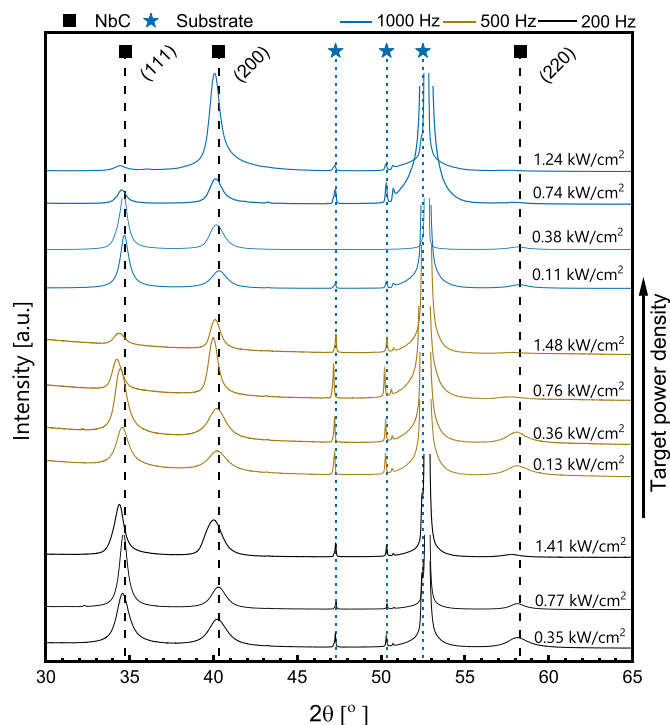
Fig. 3. Deconvoluted C1s XP spectra of two selected NbC coatings deposited at 500 Hz under different peak power densities. (a) NbC coating deposited by HiPIMS at 1.48 kW/cm² with 1.5 % pulse duty cycle. (b) NbC coating deposited by HiPIMS at 0.13 kW/cm² with 10 % pulse duty cycle.

3.3. Structural analysis

Fig. 4 presents the structural analysis by XRD for all the NbC$_x$ coatings deposited at different pulse frequencies (carried out on sapphire substrates). The diffractograms are sorted by increasing peak power densities from bottom to top and additionally grouped into the coatings grown at pulse frequencies of 200 (black lines), 500 (dark yellow), and 1000 Hz (blue lines), respectively. All NbC$_x$ films exhibit a single fcc NbC structure with no other competing crystalline phases (e.g. Nb$_2$C or pure Nb). Additionally, peak shifts towards lower 2θ can be observed for

coatings by increasing the peak power density, which is related to ion bombardment induced compressive stresses at high peak power densities. Furthermore, the preferred growth orientations in the coatings change from (111) to (200) with increasing peak power densities for coatings grown at 500 Hz and 1 kHz. As illustrated in Fig. 5 (see blue data points and axis, right-hand side), the texture coefficient for the (200) plane shows higher values for coatings deposited at 500 Hz with power density ≥ 0.75 W/cm². Moreover, the FWHM estimated for (111) and (200) peaks is plotted as a function of the peak power density for the coatings deposited at 500 Hz (see Fig. 5, left axis). The FWHM shows a decreasing trend with increasing the target peak power density. The FWHM is known to be indicative of the crystallite size, where the smaller the FWHM, the larger the crystallite size [64]. The FWHM shows a similar decreasing trend as C/Nb with increasing the target power density, indicating a correlation between the C/Nb ratio and hence the carbon content. This is in line with previous studies, highlighting the dependency of the NbC grain/crystallite size on the carbon content within the coating [13,15]. The grain size of the carbide phase correlates with the amount of carbon, whereby the grain size decreases with increasing amount of (free) carbon. This is attributed to the agglomeration of carbon at grain boundaries suppressing the growth of highly crystalline domains [15,28]. Therefore, the peak power density and hence C/Nb ratio is used as the most dominating parameter for the correlation with other properties in the following discussions, i.e. microstructure and mechanical properties.

Two coatings were chosen for detailed cross-sectional TEM investigations to describe the influence of the target peak power density on the morphology (see Fig. 6). The first NbC$_{1.43}$ coating was deposited at 500 Hz with 0.13 kW/cm² peak power density (see Fig. 6a–c). The bright-field, in addition to the HR-TEM images (Fig. 6a–b), clearly show that this coating exhibits a nanocrystalline morphology with relatively small grains embedded in an amorphous matrix. Furthermore, the selected area electron diffraction (SAED) pattern (see Fig. 6c) verifies the XRD analysis with only crystalline fcc NbC prevalent. Additionally, the SAED pattern shows continuous rings with no distinct spots, indicating the nanocrystalline nature of the microstructure with no dominant orientations. The evaluated grain size from the dark field image (based on (111) and (200) diffraction rings) was found to be 6.6 ± 2.5 nm.

The second investigated coating (NbC$_{1.01}$) was also grown at 500 Hz but under a drastically increased peak power density of 1.48 kW/cm². The influence of the increased peak power density on the microstructure is clearly visible in the BF-image of the coating cross-section (see
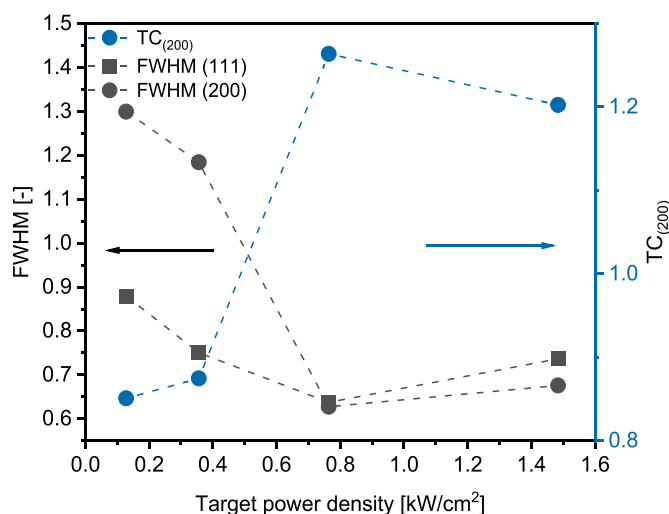

Fig. 4. X-ray diffractograms of NbC$_x$ thin films. Diffractograms are grouped with three different colours of black, yellow, and blue, corresponding to coatings deposited at HiPIMS pulse frequencies of 200, 500, and 1000 Hz, respectively. The diffractograms are labelled with the target peak power density (increasing from bottom to top). (For interpretation of the references to colour in this figure legend, the reader is referred to the web version of this article.)

Fig. 5. Full width half maximum (FWHM) of the (111) and (200) peaks, and the textural coefficient TC$_{(200)}$ of (200) plane as a function of target peak power density for NbC$_x$ coatings deposited at 500 Hz pulse frequency.
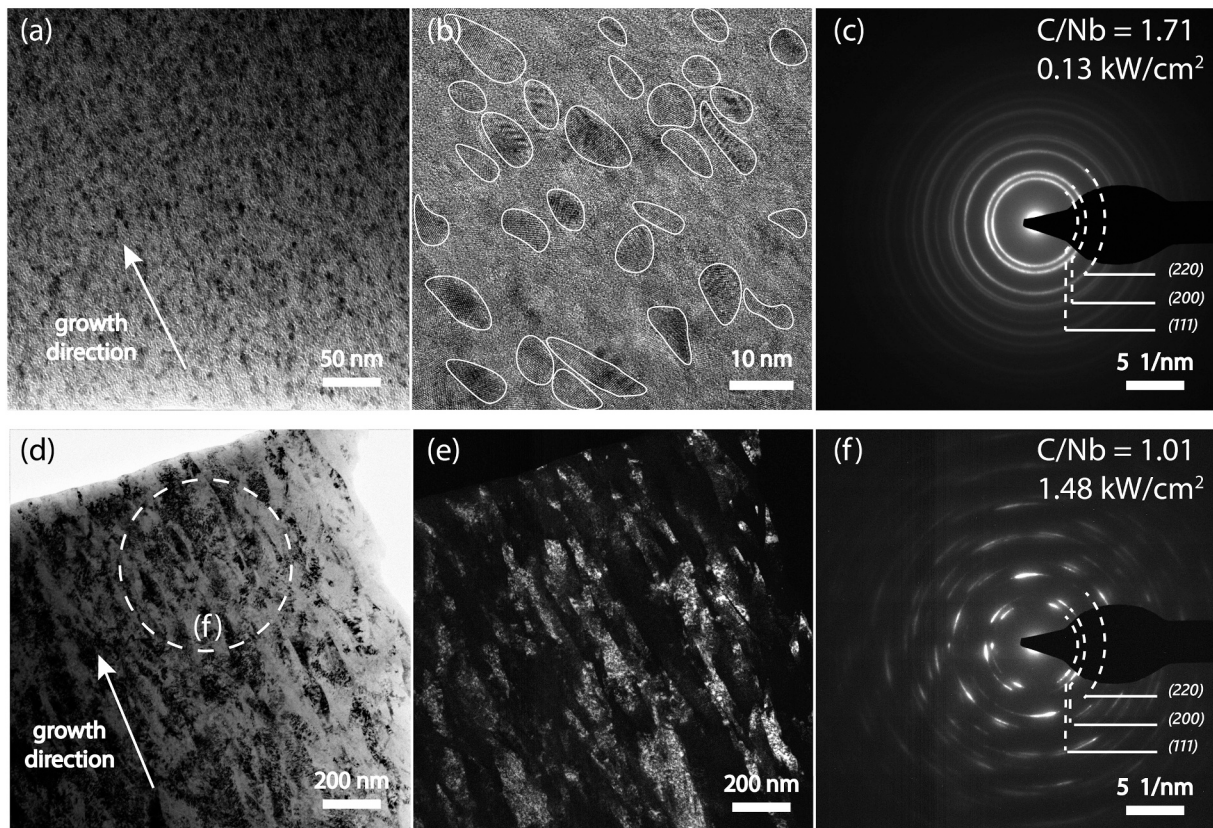
Fig. 6. Cross-sectional TEM images in bight- and dark-field modes and corresponding SAED patterns of two selected NbC coatings deposited at 500 Hz. (a), (b) and (c) present the BF-TEM micrograph, HR-TEM and SAED of NbC coating deposited by HiPIMS at 0.13 kW/cm^2 with 10 % pulse duty cycle. (d), (e) and (f) present the TEM micrographs and SAED of NbC coating deposited by HiPIMS at 1.48 kW/cm^2 with 1.5 % pulse duty cycle. The DF images were obtained using (111) and (200) diffractions. The dashed circle (f) represents the selected area for the diffraction pattern.

Fig. 6d). The coating exhibits a columnar morphology with large crystalline grains elongated in the growth direction. The average column width evaluated from the DF-image using the (111) and (200) reflections (see Fig. 6e) was found to be 65.2 ± 18.7 nm, which is much larger compared to the 6.6 ± 2.5 nm for the coating deposited at 0.13 kW/cm^2. Moreover, the SAED pattern (see Fig. 6f) confirms the single-phase cubic NbC structure in accordance with the XRD analysis. In addition, the SAED image exhibits distinct spots due to the larger grain size of this columnar crystalline coating compared to the nanocomposite coating at 0.13 kW/cm^2 having much smaller NbC$_x$ grains captured in the used aperture.

Previous studies showed that sputtered NbC films typically exhibit a nanocomposite structure comprised of a nanocrystalline carbide phase (nc-NbC$_x$) embedded in an amorphous carbon (a-C) matrix [13,15,22]. These literature findings are confirmed by our TEM investigations. As already mentioned, the C/Nb ratio in our films correlates with the target peak power density and reaches a C/Nb ratio of unity at 1.48 kW/cm^2. Consequently, the microstructure of the coating changes from a nanocomposite to a columnar structure as the peak power density increases due to the drastic reduction of C content available, which acts as an inhibitor to the columnar grain growth. The clear influence of the target peak power density on the films' composition and microstructure results in a variation of the mechanical properties of the NbC$_x$ thin films, as shown in the next section.

3.4. Mechanical properties

In Fig. 7, the residual stresses measured in the NbC$_x$ films as a function of the target peak power density is plotted. All coatings exhibit compressive stresses, obtaining more compressed states with increasing
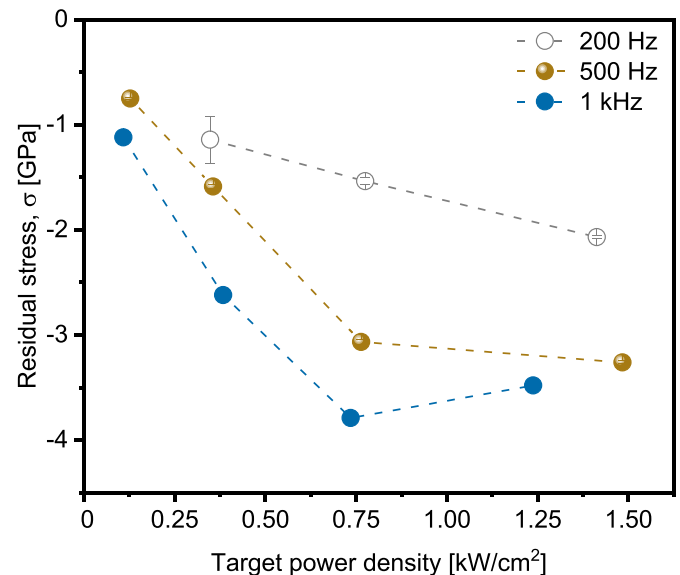
Fig. 7. Stress evolution of all NbC$_x$ coatings deposited at different pulse frequencies as a function of target power density. The error bars are relatively small compared to the symbols.

peak power densities. The stress value in the coatings deposited at a pulse frequency of 200 Hz increased slightly from -1.1 to -2.0 GPa as the power density increased from 0.35 to 1.41 kW/cm^2. Similarly, the stress value in the coatings deposited at 500 Hz increased from -0.75 to

-3.2 GPa as the power density increased from 0.13 kW/cm^2 to the maximum value of 1.48 kW/cm^2. Furthermore, the highest compressive stress values were recorded for the coatings deposited under 1 kHz with values ranging between -1.1 to -3.7 GPa. The increase in compressive residual stress with rising peak power density results from the enhanced collision cascades during the ion-assisted film growth. In addition, this process is accompanied by the introduction of point defects in the structure due to the intense ion bombardment of the growing film directly related to the utilized power density [65,66].

Fig. 8a shows the influence of the pulse frequency and target peak power density on the hardness of all deposited NbC$_x$ films. As illustrated, the hardness values show an increasing trend with increased peak power densities before plateauing around a maximum value in dependence on the pulse frequency. The hardness of the HiPIMS coatings deposited at 200 Hz increased from 27 ± 2.8 to 35.5 ± 4.3 GPa as the peak power density increased from 0.35 to 1.41 kW/cm^2. Moreover, the coatings grown at 500 Hz show a drastic increase in hardness from 28 ± 3.4 to 38.7 ± 3.6 GPa as the target peak power density raised from 0.13 to 0.76 kW/cm^2. After this substantial jump, the hardness plateaus till it reaches 37.5 ± 3 GPa at 1.48 kW/cm^2. At the highest pulse frequency of 1 kHz, the hardness of the coatings changed from 31.4 ± 2.8 to 37 ± 3.8 GPa as the power density increased from 0.11 to 0.38 kW/cm^2. Subsequently, it plateaued around this value and reached 35.5 ± 3.9 GPa at the highest peak power density of 1.24 kW/cm^2. The maximum recorded mean hardness value of 38.7 GPa was obtained for the NbC coating deposited under 0.76 kW/cm^2 at 500 Hz, obtaining a relatively low C/

Nb ratio of 1.06. The obtained hardness values exceeded those reported in the literature for reactive and non-reactive sputtered NbC$_x$ [13,15,17,20,22]. The maximum hardness for a NbC coating was reported by Mesquita et al. was 37 GPa for a film deposited using non-reactive DCMS and exhibiting an extreme residual compressive stress of 10 GPa [17]. Most of the previous studies showed that the C/Nb ratio and the amount of free carbon dramatically affect the microstructure and, consequently the hardness of the NbC$_x$ films. For example, Nedfors et al. reported a variation in the hardness from 16 to 23 GPa as the C/Nb ratio decreased from 1.59 to 0.95, while they reported lower hardness values for the non-reactively sputtered coatings due to the higher amount of amorphous carbon [15].

Nevertheless, in the present study, we observed a variation in hardness between 27 and 38 GPa strongly correlating to the C/Nb ratio and the related microstructural changes. The coating with the high C/Nb of 1.43 exhibiting a nanocomposite microstructure (see Fig. 6a) has only a hardness value of 28 GPa. However, the hardness value drastically increased to a value of 37 GPa as the microstructure changed into more columnar structures (see Fig. 6d). Glechner et al. reported in a recent study on WC$_x$ thin films the strong relation between microstructure and mechanical properties, whereas a hardness variation from 27 GPa for nanocrystalline coatings to 39 GPa for columnar crystalline coatings was observed [42]. Furthermore, the obtained hardness for the NbC$_x$ films is higher than those of bulk NbC, exhibiting 24.5 GPa, which is related to the grain size and Hall-Petch effect [67]. However, this effect is reversed below a certain grain size, and the plastic deformation occurs by grain boundary rotation and sliding (reverse Hall-Petch effect), where the reduction in grain size leads to material softening [68]. The reverse Hall-Petch effect can explain the hardness reduction in our coatings as the microstructure in the coatings changes from columnar to nanocomposite (including a-C on the grain boundaries).

Fig. 8b shows the elastic moduli as a function of the target peak power density. The elastic moduli of the NbC$_x$ films follow a similar trend as the hardness, increasing from 300 ± 5 to 402 ± 9.5 GPa with rising power density from 0.35 to 1.41 kW/cm^2 at 200 Hz. The E values for the coatings at 500 Hz started from 303 ± 10 GPa at 0.13 kW/cm^2 and peaked at 426 ± 17 GPa as the power density increased to 0.76 kW/cm^2. Furthermore, the coatings deposited at 1 kHz showed a drastic increase in the E values from 343 ± 12 to 433 ± 29 GPa as the power density slightly increased from 0.11 to 0.38 kW/cm^2. Then, the E value slightly increased with further increase in the power density till it reached 441 ± 22 GPa at the highest power density of 1.24 kW/cm^2. The obtained elastic moduli for the films deposited at high power densities with relatively low C/Nb ratio align with the reported elastic modulus for bulk NbC of 406 GPa [67]. This indicates the high crystallinity and homogeneity of these coatings since the elastic modulus is an intrinsic material property strongly dependent on the prevalent atomic bonding. However, the reported elastic modulus values for sputtered NbC coatings in the literature are in the range of 200–350 GPa [17,20,22], being comparable to the coatings with high C/Nb ratios.

Moreover, the fracture toughness of some selected coatings was determined by micro-cantilever beam bending tests. Fig. 9 presents the fracture toughness data as a function of the target peak power density for the NbC$_x$ coatings deposited at 500 Hz pulse frequency. The K$_{IC}$ value increased from 1.8 ± 0.08 to 2.5 ± 0.11 MPa·m$^{1/2}$ as the peak power density increased from 0.13 to 0.35 kW/cm^2, and it reached the maximum value of 2.78 ± 0.13 MPa·m$^{1/2}$ at 0.76 kW/cm^2 for the coating with the C/Nb ratio of 1.06. However, the minimum K$_{IC}$ value was obtained for the coating with the nanocomposite structure and, consequently highest C/Nb ratio of 1.43. The obtained low K$_{IC}$ value for the nanocomposite NbC$_{1.43}$ is related to the high fraction of free amorphous carbon phase at the grain boundaries, which features a weak bonding nature compared to the crystalline NbC phase. Moreover, the observed decrease in fracture toughness with the increasing amount of free carbon at the grain boundaries is in good agreement with the results reported in [8]. Furthermore, the K$_{IC}$ values are consistent with previous
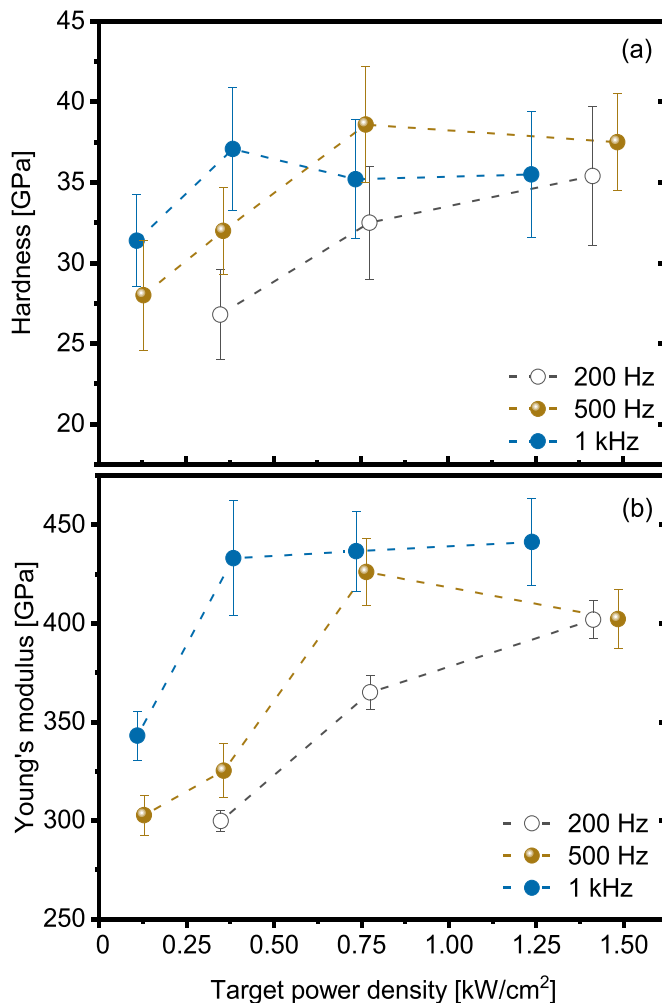

Fig. 8. (a) Hardness and (b) Elastic modulus of all NbC$_x$ coatings deposited at different pulse frequencies as a function of target power density.
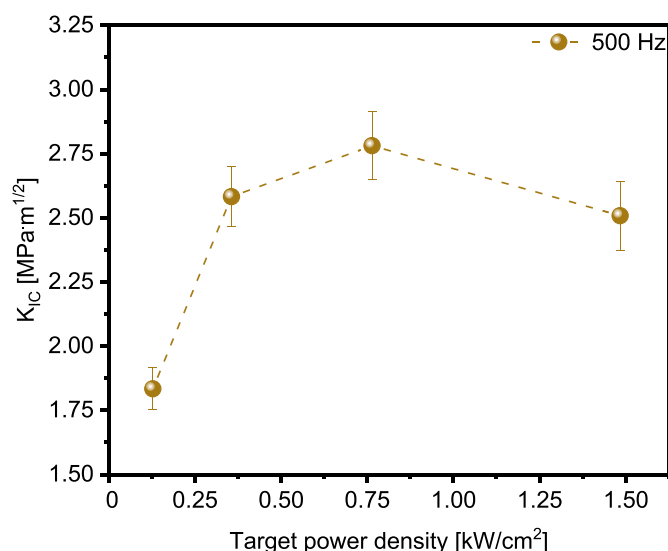
Fig. 9. Fracture toughness (K_{1C}) data as a function of target power density for the NbC_x coatings deposited by HiPIMS at 500 Hz pulse frequency.

studies on TM-Carbides correlating the fracture toughness of TMC with the valence electron concentration (VEC) [8,69–71]. By increasing VEC, the bonding character changes from a more directional covalent bonding to a more metallic bonding character, resulting in enhanced ductility and fracture characteristics. It was previously reported that HfC (VEC = 8) exhibits K_{IC} value of 1.89 MPa•$m^{1/2}$ [70], while WC (VEC = 10) reaches 3.3 MPa•$m^{1/2}$ [8]. In consequence, NbC fits this trend with 2.78 ± 0.13 MPa•$m^{1/2}$ for $NbC_{1.06}$, obtaining a VEC of 9.

4. Conclusions

Within this study, we have demonstrated that the chemical composition, microstructure, and mechanical properties of NbC_x thin films grown by HiPIMS can be controlled by the applied target peak power density. Three series of NbC_x coatings have been deposited at pulse frequencies of 200, 500, and 1000 Hz. By decreasing the HiPIMS pulse duty cycle from 10 to 1.5 %, while maintaining all other parameters constant, the peak power density varied from 0.11 to 1.48 kW/cm^2. This ion-assisted change of the growth conditions leads to a drastic reduction of the C/Nb (from 1.52 to 0.99) within the fcc-structured films. Concurrently, the microstructure of the coatings changed from a nanocomposite morphology with an estimated NbC_x grain size of 6.6 ± 2.5 nm at 0.13 kW/cm^2 ($NbC_{1.43}$) into a columnar structure with an average column width of 65.2 ± 18.7 nm at 1.48 kW/cm^2 ($NbC_{1.01}$). The drastic change of the C/Nb ratio and subsequently the microstructure with increasing peak power density is based on the enhanced growth conditions, dominated by ions rather than neutrals. The related changes in chemical composition and microstructure also strongly influence the mechanical properties of the NbC_x films. The maximum hardness values of around 38 GPa were obtained for the nearly stoichiometric films. The fracture toughness also correlates with the C/Nb ratio, whereas a high amount of free carbon – a prerequisite for a nanocrystalline morphology with a C-rich amorphous grain boundary phase – leads to lower K_{IC} values, i.e. 1.8 ± 0.08 MPa•$m^{1/2}$ for $NbC_{1.43}$ at 0.13 kW/cm^2 compared to 2.78 ± 0.13 MPa•$m^{1/2}$ for the highly columnar $NbC_{1.06}$ coating (0.76 kW/cm^2).

In summary, this study highlights the versatile possibilities in non-reactive HiPIMS deposition of NbC_x coatings, allowing for a distinct control of the film stoichiometry, microstructure, and mechanical properties, by simply tuning the HiPIMS pulse parameters.

CRediT authorship contribution statement

A. Bahr: Conceptualization, Investigation, Writing – original draft. **T. Glechner:** Writing – review & editing. **T. Wojcik:** Investigation. **A. Kirnbauer:** Investigation. **M. Sauer:** Investigation. **A. Foelske:** Resources. **O. Hunold:** Resources, Writing – review & editing. **J. Ramm:** Resources, Writing – review & editing. **S. Kolozsvári:** Resources, Writing – review & editing. **E. Ntemou:** Investigation. **E. Pitthan:** Investigation. **D. Primetzhofer:** Resources. **H. Riedl:** Supervision, Writing – review & editing. **R. Hahn:** Supervision, Writing – review & editing.

Declaration of competing interest

The authors declare that they have no known competing financial interests or personal relationships that could have appeared to influence the work reported in this paper.

Data availability

Data will be made available on request.

Acknowledgments

Appendix A. Supplementary data

Supplementary data to this article can be found online at https://doi.org/10.1016/j.surfcoat.2022.128674.

References

[1] H.O. Pierson, Handbook of Refractory Carbides and Nitrides, in: William Andrew Publishing, Westwood, NJ, 1996, pp. 8–16.

[2] W.S. Williams, Electrical properties of hard materials, Int. J. Refract. Met. Hard Mater. 17 (1999) 21–26.

[3] M. Samuelsson, K. Sarakinos, H. Högberg, E. Lewin, U. Jansson, B. Wälivaara, H. Ljungcrantz, U. Helmersson, Growth of ti-C nanocomposite films by reactive high power impulse magnetron sputtering under industrial conditions, Surf. Coat. Technol. 206 (2012) 2396–2402.

[4] H. Lasfargues, T. Glechner, C.M. Koller, V. Paneta, D. Primetzhofer, S. Kolozsvári, D. Holec, H. Riedl, P.H. Mayrhofer, Non-reactively sputtered ultra-high temperature hf-C and ta-C coatings, Surf. Coat. Technol. 309 (2017) 436–444.

[5] A. Gilewicz, K. Mydłowska, J. Ratajski, Ł. Szparaga, P. Bartosik, P. Kochmański, R. Jędrzejewski, Structural, mechanical and tribological properties of ZrC thin films deposited by magnetron sputtering, Vacuum 169 (2019).

[6] H. Riedl, T. Glechner, T. Wojcik, N. Koutná, S. Kolozsvári, V. Paneta, D. Holec, D. Primetzhofer, P.H. Mayrhofer, Influence of carbon deficiency on phase formation and thermal stability of super-hard TaCy thin films, Scr. Mater. 149 (2018) 150–154.

[7] M.-H. Ding, H.-S. Zhang, C. Zhang, X. Jin, Characterization of ZrC coatings deposited on biomedical 316L stainless steel by magnetron sputtering method, Surf. Coat. Technol. 224 (2013) 34–41.

[8] T. Glechner, R. Hahn, L. Zauner, S. Rißlegger, A. Kirnbauer, P. Polcik, H. Riedl, Structure and mechanical properties of reactive and non-reactive sputter deposited WC based coatings, J. Alloys Compd. 885 (2021) 161129.

[9] Y. Zhong, X. Xia, F. Shi, J. Zhan, J. Tu, H.J. Fan, Transition metal carbides and nitrides in energy storage and conversion, Adv. Sci. (Weinh) 3 (2016) 1500286.

[10] Y.N. Regmi, G.R. Waetzig, K.D. Duffee, S.M. Schmuecker, J.M. Thode, B. M. Leonard, Carbides of group IVAVA and VIA transition metals as alternative HER and ORR catalysts and support materials, Journal of Materials Chemistry A 3 (2015) 10085–10091.

[11] F. Karimi, B.A. Peppley, Metal carbide and oxide supports for iridium-based oxygen evolution reaction electrocatalysts for polymer-electrolyte-membrane water electrolysis, Electrochim. Acta 246 (2017) 654–670.

[12] C.N. Zoita, L. Braic, A. Kiss, M. Braic, Characterization of NbC coatings deposited by magnetron sputtering method, Surf. Coat. Technol. 204 (2010) 2002–2005.

[13] N. Nedfors, O. Tengstrand, E. Lewin, A. Furlan, P. Eklund, L. Hultman, U. Jansson, Structural, mechanical and electrical-contact properties of nanocrystalline-NbC/ amorphous-C coatings deposited by magnetron sputtering, Surf. Coat. Technol. 206 (2011) 354–359.

[14] K. Zhang, M. Wen, Q.N. Meng, C.Q. Hu, X. Li, C. Liu, W.T. Zheng, Effects of substrate bias voltage on the microstructure, mechanical properties and tribological behavior of reactive sputtered niobium carbide films, Surf. Coat. Technol. 212 (2012) 185–191.

[15] N. Nedfors, O. Tengstrand, A. Flink, A.M. Andersson, P. Eklund, L. Hultman, U. Jansson, Reactive sputtering of NbCx-based nanocomposite coatings: an up-scaling study, Surf. Coat. Technol. 253 (2014) 100–108.

[16] M. Woydt, H. Mohrbacher, The use of niobium carbide (NbC) as cutting tools and for wear resistant tribosystems, Int. J. Refract. Met. Hard Mater. 49 (2015) 212–218.

[17] R.A. Mesquita, C.A. Schuh, Tool steel coatings based on niobium carbide and carbonitride compounds, Surf. Coat. Technol. 207 (2012) 472–479.

[18] P. Zhang, C. Hao, Y. Han, F. Du, H. Wang, X. Wang, J. Sun, Electrochemical behavior and surface conductivity of NbC modified ti bipolar plate for proton exchange membrane fuel cell, Surf. Coat. Technol. 397 (2020).

[19] A. Amaya, O. Piamba, J. Olaya, Improvement of corrosion resistance for gray cast iron in palm biodiesel application using thermoreactive diffusion niobium carbide (NbC) coating, Coatings 8 (2018).

[20] N. Sala, M.D. Abad, J.C. Sánchez-López, M. Cruz, J. Caro, C. Colominas, Tribological performance of nb-C thin films prepared by DC and HiPIMS, Mater. Lett. 277 (2020).

[21] M.Y. Liao, Y. Gotoh, H. Tsuji, J. Ishikawa, Compound-target sputtering for niobium carbide thin-film deposition, J. Vac. Sci. Technol., B: Microelectron. Nanometer Struct.–Process., Meas., Phenom. 22 (2004).

[22] L. Yate, L. Emerson Coy, G. Wang, M. Beltrán, E. Díaz-Barriga, E.M. Saucedo, M. A. Ceniceros, K. Załęski, I. Llarena, M. Möller, R.F. Ziolo, Tailoring mechanical properties and electrical conductivity of flexible niobium carbide nanocomposite thin films, RSC Adv. 4 (2014) 61355–61362.

[23] A. Bendavid, P.J. Martin, T.J. Kinder, E.W. Preston, The deposition of NbN and NbC thin films by filtered vacuum cathodic arc deposition, Surf. Coat. Technol. 163–164 (2003) 347–352.

[24] D. Ferro, J.V. Rau, A. Generosi, V. Rossi Albertini, A. Latini, S.M. Barinov, Electron beam deposited VC and NbC thin films on titanium: hardness and energy-dispersive X-ray diffraction study, Surf. Coat. Technol. 202 (2008) 2162–2168.

[25] V.L.S. Teixeira da Silva, M. Schmal, S.T. Oyama, Niobium carbide synthesis from niobium oxide: study of the synthesis conditions, kinetics, and solid-state transformation mechanism, J. Solid State Chem. 123 (1996) 168–182.

[26] K.-W. Kim, B. Kim, S. Lee, T. Nasir, H. Lim, I. Choi, B. Jeong, J. Lee, H. Yu, J.-Y. Choi, Growth of NbC thin film using CH4 as a carbon source and reducing agent, Coatings 8 (2018).

[27] Q. Li, Y. Lei, H. Fu, Laser cladding in-situ NbC particle reinforced fe-based composite coatings with rare earth oxide addition, Surf. Coat. Technol. 239 (2014) 102–107.

[28] U. Jansson, E. Lewin, Sputter deposition of transition-metal carbide films — a critical review from a chemical perspective, Thin Solid Films 536 (2013) 1–24.

[29] K. Sarakinos, L. Martinu, 8 - Synthesis of thin films and coatings by high power impulse magnetron sputtering, in: D. Lundin, T. Minea, J.T. Gudmundsson (Eds.), High Power Impulse Magnetron Sputtering, Elsevier, 2020, pp. 333–374.

[30] V. Kouznetsov, K. Macák, J.M. Schneider, U. Helmersson, I. Petrov, A novel pulsed magnetron sputter technique utilizing very high target power densities, Surf. Coat. Technol. 122 (1999) 290–293.

[31] A. Anders, Discharge physics of high power impulse magnetron sputtering, Surf. Coat. Technol. 205 (2011) S1–S9.

[32] K. Sarakinos, J. Alami, S. Konstantinidis, High power pulsed magnetron sputtering: a review on scientific and engineering state of the art, Surf. Coat. Technol. 204 (2010) 1661–1684.

[33] J.T. Gudmundsson, N. Brenning, D. Lundin, U. Helmersson, High power impulse magnetron sputtering discharge, J. Vac. Sci. Technol. A 30 (2012), 030801.

[34] B. Bakhit, I. Petrov, J.E. Greene, L. Hultman, J. Rosén, G. Greczynski, Controlling the B/Ti ratio of TiBx thin films grown by high-power impulse magnetron sputtering, J. Vac. Sci. Technol. A 36 (2018).

[35] G. Greczynski, S. Mráz, H. Ruess, M. Hans, J. Lu, L. Hultman, J.M. Schneider, Extended metastable Al solubility in cubic VAlN by metal-ion bombardment during pulsed magnetron sputtering: film stress vs subplantation, J. Appl. Phys. 122 (2017).

[36] G. Greczynski, S. Mráz, J.M. Schneider, L. Hultman, Metal-ion subplantation: a game changer for controlling nanostructure and phase formation during film growth by physical vapor deposition, J. Appl. Phys. 127 (2020).

[37] L. Zauner, P. Ertelthaler, T. Wojcik, H. Bolvardi, S. Kolozsvári, P.H. Mayrhofer, H. Riedl, Reactive HiPIMS deposition of ti-Al-N: influence of the deposition parameters on the cubic to hexagonal phase transition, Surf. Coat. Technol. 382 (2020), 125007.

[38] L. Zauner, A. Bahr, T. Kozák, J. Čapek, T. Wojcik, O. Hunold, S. Kolozsvári, P. Zeman, P.H. Mayrhofer, H. Riedl, Time-averaged and time-resolved ion fluxes related to reactive HiPIMS deposition of ti-Al-N films, Surf. Coat. Technol. 424 (2021), 127638.

[39] S. Karimi Aghda, D. Music, Y. Unutulmazsoy, H.H. Sua, S. Mráz, M. Hans, D. Primetzhofer, A. Anders, J.M. Schneider, Unravelling the ion-energy-dependent structure evolution and its implications for the elastic properties of (V, Al)N thin films, Acta Mater. 214 (2021), 117003.

[40] J.C. Sánchez-López, A. Caro, G. Alcalá, T.C. Rojas, Tailoring CrNx stoichiometry and functionality by means of reactive HiPIMS, Surf. Coat. Technol. 401 (2020), 126235.

[41] P. Souček, J. Daniel, J. Hnilica, K. Bernátová, L. Zábranský, V. Buršíková, M. Stupavská, P. Vašina, Superhard nanocomposite nc-TiC/a-C: H coatings: the effect of HiPIMS on coating microstructure and mechanical properties, Surf. Coat. Technol. 311 (2017) 257–267.

[42] T. Glechner, C. Tomastik, E. Badisch, P. Polcik, H. Riedl, Influence of WC/C target composition and bias potential on the structure-mechanical properties of non-reactively sputtered WC coatings, Surf. Coat. Technol. 432 (2022), 128036.

[43] T. Glechner, H.G. Oemer, T. Wojcik, M. Weiss, A. Limbeck, J. Ramm, P. Polcik, H. Riedl, Influence of Si on the oxidation behavior of TM-si-B2±z coatings (TM = Ti, Cr, Hf, Ta, W), Surf. Coat. Technol. 128178 (2022).

[44] P. Ström, D. Primetzhofer, Ion beam tools for nondestructive in-situ and in-operando composition analysis and modification of materials at the tandem Laboratory in Uppsala, J. Instrum. 17 (2022) P04011.

[45] M. Janson, CONTES Instruction Manual, Uppsala University, Uppsala, Sweden, 2004.

[46] K. Arstila, J. Julin, M.I. Laitinen, J. Aalto, T. Konu, S. Kärkkäinen, S. Rahkonen, M. Raunio, J. Itkonen, J.P. Santanen, T. Tuovinen, T. Sajavaara, Potku – new analysis software for heavy ion elastic recoil detection analysis, Nucl. Instrum. Methods Phys. Res., Sect. B 331 (2014) 34–41.

[47] P. Petersson, M. Rubel, G. Possnert, A combined segmented anode gas ionization chamber and time-of-flight detector for heavy ion elastic recoil detection analysis, Rev Sci Instrum 87 (2016), 103303.

[48] J.A. Leavitt, L.C. McIntyre, M.D. Ashbaugh, J.G. Oder, Z. Lin, B. Dezfouly-Arjomandy, Cross sections for 170.5° backscattering of 4He from oxygen for 4He energies between 1.8 and 5.0 MeV, Nucl. Instrum. Methods Phys. Res., Sect. B 44 (1990) 260–265.

[49] M. Mayer, Improved physics in SIMNRA 7, Nucl. Instrum. Methods Phys. Res., Sect. B 332 (2014) 176–180.

[50] M.V. Moro, R. Holeňák, L. Zendejas Medina, U. Jansson, D. Primetzhofer, Accurate high-resolution depth profiling of magnetron sputtered transition metal alloy films containing light species: a multi-method approach, Thin Solid Films 686 (2019), 137416.

[51] J.H. Scofield, Hartree-slater subshell photoionization cross-sections at 1254 and 1487 eV, J. Electron Spectrosc. Relat. Phenom. 8 (1976) 129–137.

[52] W.C. Oliver, G.M. Pharr, An improved technique for determining hardness and elastic modulus using load and displacement sensing indentation experiments, J. Mater. Res. 7 (1992) 1564–1583.

[53] A.C. Fischer-Cripps, Critical review of analysis and interpretation of nanoindentation test data, Surf. Coat. Technol. 200 (2006) 4153–4165.

[54] H.M. Ledbetter, S. Chevacharoenkul, R.F. Davis, Monocrystal elastic constants of NbC, J. Appl. Phys. 60 (1986) 1614–1617.

[55] K. Matoy, H. Schönherr, T. Detzel, T. Schöberl, R. Pippan, C. Motz, G. Dehm, A comparative micro-cantilever study of the mechanical behavior of silicon based passivation films, Thin Solid Films 518 (2009) 247–256.

[56] S. Brinckmann, C. Kirchlechner, G. Dehm, Stress intensity factor dependence on anisotropy and geometry during micro-fracture experiments, Scr. Mater. 127 (2017) 76–78.

[57] S. Brinckmann, K. Matoy, C. Kirchlechner, G. Dehm, On the influence of microcantilever pre-crack geometries on the apparent fracture toughness of brittle materials, Acta Mater. 136 (2017) 281–287.

[58] G.Y. Yushkov, A. Anders, Origin of the delayed current onset in high-power impulse magnetron sputtering, IEEE Trans. Plasma Sci. 38 (2010) 3028–3034.

[59] D. Lundin, N. Brenning, D. Jädernäs, P. Larsson, E. Wallin, M. Lattemann, M. A. Raadu, U. Helmersson, Transition between the discharge regimes of high power impulse magnetron sputtering and conventional direct current magnetron sputtering, Plasma Sources Sci. Technol. 18 (2009).

[60] S. Mráz, J. Emmerlich, F. Weyand, J.M. Schneider, Angle-resolved evolution of the composition of Cr–Al–C thin films deposited by sputtering of a compound target, J. Phys. D. Appl. Phys. 46 (2013), 135501.

[61] M.G. Cuppari, S.F. Santos, Physical properties of the NbC carbide, Metals 6 (2016).

[62] J. Alami, K. Sarakinos, F. Uslu, M. Wuttig, On the relationship between the peak target current and the morphology of chromium nitride thin films deposited by reactive high power pulsed magnetron sputtering, J. Phys. D. Appl. Phys. 42 (2008), 015304.

[63] W.M. Haynes, in: CRC Handbook of Chemistry and Physics, 95th Edition, CRC press, 2014, p. 17.

[64] A. Guinier, in: X-ray Diffraction in Crystals, Imperfect Crystals, and Amorphous Bodies, Dover Publications, 1994, pp. 234–236.

[65] I. Petrov, P.B. Barna, L. Hultman, J.E. Greene, Microstructural evolution during film growth, J. Vac. Sci. Technol. A 21 (2003) S117–S128.

[66] G. Greczynski, J. Lu, M. Johansson, J. Jensen, I. Petrov, J.E. Greene, L. Hultman, Selection of metal ion irradiation for controlling Ti1−xAlxN alloy growth via hybrid HIPIMS/magnetron co-sputtering, Vacuum 86 (2012) 1036–1040.

[67] L. Wu, Y. Wang, Z. Yan, J. Zhang, F. Xiao, B. Liao, The phase stability and mechanical properties of Nb–C system: using first-principles calculations and nano-indentation, J. Alloys Compd. 561 (2013) 220–227.

[68] J. Schiøtz, F.D. Di Tolla, K.W. Jacobsen, Softening of nanocrystalline metals at very small grain sizes, Nature 391 (1998) 561–563.

[69] K. Balasubramanian, S.V. Khare, D. Gall, Valence electron concentration as an indicator for mechanical properties in rocksalt structure nitrides, carbides and carbonitrides, Acta Mater. 152 (2018) 175–185.

[70] T. Glechner, S. Lang, R. Hahn, M. Alfreider, V. Moraes, D. Primetzhofer, J. Ramm, S. Kolozsvári, D. Kiener, H. Riedl, Correlation between fracture characteristics and valence electron concentration of sputtered hf-C-N based thin films, Surf. Coat. Technol. 399 (2020), 126212.

[71] T. Glechner, R. Hahn, T. Wojcik, D. Holec, S. Kolozsvári, H. Zaid, S. Kodambaka, P. H. Mayrhofer, H. Riedl, Assessment of ductile character in superhard ta-C-N thin films, Acta Mater. 179 (2019) 17–25.